npj | 2D Materials and Applications

www.nature.com/npj2dmaterials

ARTICLE OPEN

Check for updates

2D-MoS_2 goes 3D: transferring optoelectronic properties of 2D MoS_2 to a large-area thin film

Melanie Timpel[1,2✉], Giovanni Ligorio[3], Amir Ghiami[1,4], Luca Gavioli[5], Emanuele Cavaliere[5], Andrea Chiappini[6], Francesca Rossi[7], Luca Pasquali[8,9,10], Fabian Gärisch[3], Emil J. W. List-Kratochvil[3,11], Petr Nozar[1], Alberto Quaranta[2], Roberto Verucchi[1] and Marco V. Nardi[1✉]

The ongoing miniaturization of electronic devices has boosted the development of new post-silicon two-dimensional (2D) semiconductors, such as transition metal dichalcogenides, one of the most prominent materials being molybdenum disulfide (MoS_2). A major obstacle for the industrial production of MoS_2-based devices lies in the growth techniques. These must ensure the reliable fabrication of MoS_2 with tailored 2D properties to allow for the typical direct bandgap of 1.9 eV, while maintaining large-area growth and device compatibility. In this work, we used a versatile and industrially scalable MoS_2 growth method based on ionized jet deposition and annealing at 250 °C, through which a 3D stable and scalable material exhibiting excellent electronic and optical properties of 2D MoS_2 is synthesized. The thickness-related limit, i.e., the desired optical and electronic properties being limited to 2D single/few-layered MoS_2, was overcome in the thin film through the formation of encapsulated highly crystalline 2D MoS_2 nanosheets exhibiting a bandgap of 1.9 eV and sharp optical emission. The newly synthesized 2D-in-3D MoS_2 structure will facilitate device compatibility of 2D materials and confer superior optoelectronic device function.

npj 2D Materials and Applications (2021)5:64 ; https://doi.org/10.1038/s41699-021-00244-x

INTRODUCTION

Two-dimensional (2D) transition metal dichalcogenides (TMDCs) such as MoS_2 hold great potential for applications in next-generation optoelectronic devices, e.g., by overcoming the intrinsic limitation of graphene-related to its semi-metal character (i.e., zero bandgap)[1]. Unlike graphene, the bandgap of 2D TMDCs can be tuned from indirect to direct by varying the number of layers[2–4]. Moreover, the properties of MoS_2 such as chemical reactivity and electronic configuration make it a preferential candidate for a wide range of applications ranging from catalysis, such as water splitting and hydrogen generation for energy storage and harvesting[5–7] to biomedicine for cancer therapy and bone regeneration[8–10]. Hence, many synthesis routes have been recently pursued to grow large-area 2D MoS_2. Top-down approaches such as exfoliation methods[11–13], present severe limitations due to the small size of exfoliated layers and cumbersome large-area scalability, and due to the poor control of their morphological and structural properties. Bottom-up methods include chemical vapour deposition (CVD)[14–16], thermal decomposition of Mo-based precursors[17,18] and sol−gel derived growth[19,20], physical vapour deposition (PVD)[21], in particular pulsed laser deposition (PLD)[22–24] and magnetron sputtering[25,26]. As a matter of fact, most of these bottom-up techniques still lack industrial scalability for simple and low-cost production of 2D MoS_2 with uniform and reproducible material properties (e.g., stoichiometry, high mobility). A major open issue lies in the nature of the substrates employed during the growth (e.g., pre-patterned, flexible, metallic, etc.), often limiting the processing temperature and the film size. Furthermore, the 2D material's fragility is challenging for the integration into the current device technology. For instance, if 2D materials are used as electrodes (usually in form of a single or few-layered flake), the devices can easily fail due to disruption of the layer integrity. These problems call for a synthesis method able to provide 2D materials possessing the desired properties, but with the strength of the bulk material.

A competitive approach for low-cost and industrially scalable growth of materials is the ionized jet deposition (IJD), which is a pulsed electron deposition method developed by Noivion S.r.l. (Italy)[27–29] and optimized for MoS_2 deposition in collaboration with the IMEM-CNR institute (Italy)[30]. It is based on an ionized gas jet, which acts as source and carrier gas of pulsed electrons and in a later step as carrier gas (plasma) for the material to be deposited. Briefly, after ultra-short electric discharges in the MW range are generated by a controlled and geometrically confined cascade ionization[31], the dense and highly energetic pulsed electrons are directed towards a solid target constituted by the material-of-interest, where they generate a superficial explosion with consequent emission (ablation) of the material that finally condenses on a substrate kept in front of the target. Using a single IJD source, uniform deposition of diameters up to 10 cm (e.g., 4-inch wafer) can be realized; by assembling several IJD sources that are mounted in-line, surfaces can be uniformly coated without any size limitations (more details about the IJD technique can be found in Supplementary Fig. 1). By controlling the deposition parameters[30], it is possible to tune the stoichiometry of the deposited film and replicate one of the targets. In contrast

[1]IMEM-CNR, Institute of Materials for Electronics and Magnetism, Trento Unit c/o Fondazione Bruno Kessler, Trento, Italy. [2]Department of Industrial Engineering, University of Trento, Trento, Italy. [3]Institut für Physik, Institut für Chemie & IRIS Adlershof, Humboldt-Universität zu Berlin, Berlin, Germany. [4]Department of Chemistry, Life Science and Environmental Sustainability—University of Parma, Parma, Italy. [5]Interdisciplinary Laboratories for Advanced Materials Physics (i-LAMP) and Dipartimento di Matematica e Fisica, Università Cattolica del Sacro Cuore, Brescia, Italy. [6]CNR-IFN, CSMFO Lab & FBK Photonics Unit, Trento, Italy. [7]IMEM-CNR, Institute of Materials for Electronics and Magnetism, Parma, Italy. [8]IOM-CNR Institute, Trieste, Italy. [9]University of Modena e Reggio Emilia, Engineering Department, Modena, Italy. [10]Department of Physics, University of Johannesburg, Johannesburg, South Africa. [11]Helmholtz-Zentrum Berlin für Materialien und Energie GmbH, Berlin, Germany. ✉email: melanie.timpel@imem.cnr.it; marcovittorio.nardi@imem.cnr.it

to PLD, where a complex and expensive laser source and ultra-high vacuum (UHV) conditions are needed[22–24], the pulsed electron source of IJD operates in vacuum with 10^{-7} mbar base pressure. These vacuum conditions make IJD a compact, cost-competitive, and industrially up-scalable technique, compatible with current micro- and nanofabrication processes (e.g., top-down lithography, wiring, bonding, and micro-/nanomanipulation), providing high deposition rates, low substrate heating, and a great tunability of the growth parameters. Due to material ablation instead of sputtering, almost any material can be deposited with very efficient material/target use. The IJD method has been successfully used to grow thin films from a wide range of complex materials on various substrates, such as hard metal carbides and nitrides on silicon, aluminium alloy and stainless steel substrates[32], yttria-stabilized zirconia on SiO_2, borosilicate, titanium and poly(ether ether ketone)[33], tin sulfide layers on soda-lime glass[34], soft polymers on stainless steel and glass substrates[35], and bone apatite-like films on silicon[36,37]. Hence, the IJD technique represents a versatile, very safe, and low-temperature process, which can be explored for TMDC growth, e.g., to obtain stoichiometric and crystalline 2H-MoS_2 without the use of hazardous gases such as hydrogen and sulfur, and carbon compounds, or other molecules (often used as catalysators in the synthesis).

In this contribution, we demonstrate for the first time the growth of large-area MoS_2 thin films employing IJD. The material is very attractive for technological and industrial-relevant scalable applications due to the relatively low temperature needed for the annealing process (250 °C), which is compatible with some high-performance flexible polymers such as polyimide. The films with thicknesses of ~200 nm remarkably display electronic and optical properties like encapsulated 2D MoS_2 (single or few layers). More specifically, they exhibit a bandgap of 1.86 eV and well-resolved photoluminescence spectra with an excitonic linewidth of less than 10 meV. These properties are given by the 3D structure obtained via the IJD thin film growth and subsequent annealing. The deposited material is initially composed of an amorphous film of Mo_xS_y nanoclusters, which rearrange after annealing into crystalline hexagonal and p-doped 2D MoS_2 nanosheets (1–4 layers) encapsulated by amorphous, stoichiometric MoS_2. The high quality of the IJD-grown MoS_2 thin film for electronic applications is demonstrated on a memristive device.

RESULTS

Sample preparation

The MoS_2 thin films (with thicknesses of ~ 200 nm) were grown on Pt and Au/Si_3N_4 substrates via IJD (see Supplementary Fig. 1 for details on deposition and geometry) and subsequently annealed at low temperature. The formation of a stoichiometric crystalline MoS_2 structure is obtained at the annealing temperature of 250 °C in combination with the optimization of the IJD parameters.

Chemical and morphological properties

The X-ray photoemission spectroscopy (XPS) chemical analysis of the MoS_2 thin films is reported in Fig. 1a–c, where representative spectra (survey, Mo 3d + S 2s and S 2p core levels, respectively) are shown. The wide energy range spectrum is dominated by Mo and S species. Small contributions arising from carbon and oxygen are mainly due to residual gases in the IJD chamber (pressure during deposition: 10^{-3}–10^{-5} mbar) conditions. It should be noted that high vacuum conditions are compatible with scalable applications, differently from other PVD techniques working in UHV. The spectral features of the Mo 3d peak in Fig. 1b show that Mo has a 4+ oxidation state, indicating successful synthesis of MoS_2. In particular, the Mo $3d_{5/2}$ and $3d_{3/2}$ peaks are located at binding energies (BEs) of 228.9 and 232.2 eV, respectively, and the S 2s peak is observed at 226.3 eV. The peaks at BE of 161.8 and 162.9 eV correspond to the S $2p_{3/2}$ and $2p_{1/2}$ of MoS_2, respectively (see Fig. 1c). From quantitative analysis, the atomic ratio S/Mo is 2.11 ± 0.10, in good agreement with the nominal expected one. It is noteworthy that the Mo 3d and S 2p core levels of the annealed MoS_2 thin film are shifted by 0.6 eV to lower BEs with respect to the as-deposited case (Supplementary Fig. 1), indicating a change in the chemical configuration and electronic structure of the MoS_2 thin film after annealing. Overall, the spectra exhibit a narrow Mo 3d and S 2p line shape (as evaluated via full width at half maximum, FWHM = 1.0 and 0.9 eV, respectively), suggesting that the optimized parameters for IJD and annealing enable the formation of chemically pure MoS_2. Figure 1d shows an X-ray diffraction (XRD) scan to investigate the crystalline structure of the MoS_2 films. The peaks are assigned to the MoS_2 crystal planes according to ref. [38]. The interlayer distance obtained via the Bragg equation results is 6.19 Å, in excellent agreement with the standard hexagonal 2H-MoS_2 crystal (6.14 Å)[39]. The surface morphology of the deposited films obtained by atomic force microscopy (AFM) is shown in Fig. 1e. The representative topography image (1 μm × 1 μm) shows that the MoS_2 thin film exhibits a continuous surface with nm-sized protrusions and pores. Large area AFM and scanning electron microscopy (SEM) images of the MoS_2 surface are displayed in Supplementary Fig. 2, evidencing the formation of large-area homogeneous thin films.

Optical properties

Photoluminescence (PL) measurements (excitation wavelength of $\lambda = 532$ nm) were performed to investigate the optical properties of the IJD-grown MoS_2 thin films. PL allows to distinguish bulk (3D) from 2D MoS_2, thanks to the indirect-to-direct bandgap semiconductor transition that MoS_2 undergoes when confined in the mono- and few-layer regime. Room temperature PL spectra of 2D MoS_2 are typically observed as a broad peak centred at ~650 nm (1.9 eV), commonly ascribed to A exciton complexes, i.e., a convolution of neutral (X^0) and red-shifted charged excitons (trion, T) with linewidths around 50−100 meV[2,40–43], whereas the X^0 and T excitons are resolved in low-temperature PL spectra of encapsulated 2D-MoS_2 reaching linewidths around 10 meV[44–46]. Fig. 2a reports representative PL spectra collected on a deposited MoS_2 thin film before and after annealing. Whereas before annealing no PL signal is detected (black curve in Fig. 2a), after annealing the MoS_2 remarkably displays a PL emission spectrum consisting of a minor X^0 peak centred at 1902 meV (652 nm) and a sharp peak stemming from charged excitons (labelled as T in Fig. 2a) located 47 meV below X^0 with a linewidth of less than 10 meV. In addition, a third peak (X^L) located 101 meV below X^0 is observed, which has been recently ascribed to atomic defects and vacancies in the MoS_2 structure[47].

Additional PL spectra acquired in different sample positions, as well as with another excitation wavelength ($\lambda = 632$ nm) (Supplementary Fig. 3a, b), confirm the well-resolved PL emission despite the thickness of the samples.

Non-resonant Raman spectra ($\lambda = 532$ nm) were collected on the MoS_2 thin film before and after annealing (Fig. 2b). The spectra reveal two typical Raman active modes of hexagonal MoS_2, namely in-plane vibrations (E^1_{2g}) at 383.0 and 384.5 cm^{-1} before and after annealing, respectively, and out-of-plane (A_{1g}) vibrations at 408.0 and 403.2 cm^{-1}, respectively. Similar to the PL emission, the wavenumbers difference between the two Raman modes is also a useful parameter to indicate confinement of MoS_2 from 3D to 2D as the difference decreases during this process[48,49]. Before annealing, the difference between the E^1_{2g} and A_{1g} modes is equal to 25.0 cm^{-1}, typical bulk MoS_2, whereas for the annealed MoS_2 thin film, the measured difference decreases and, although

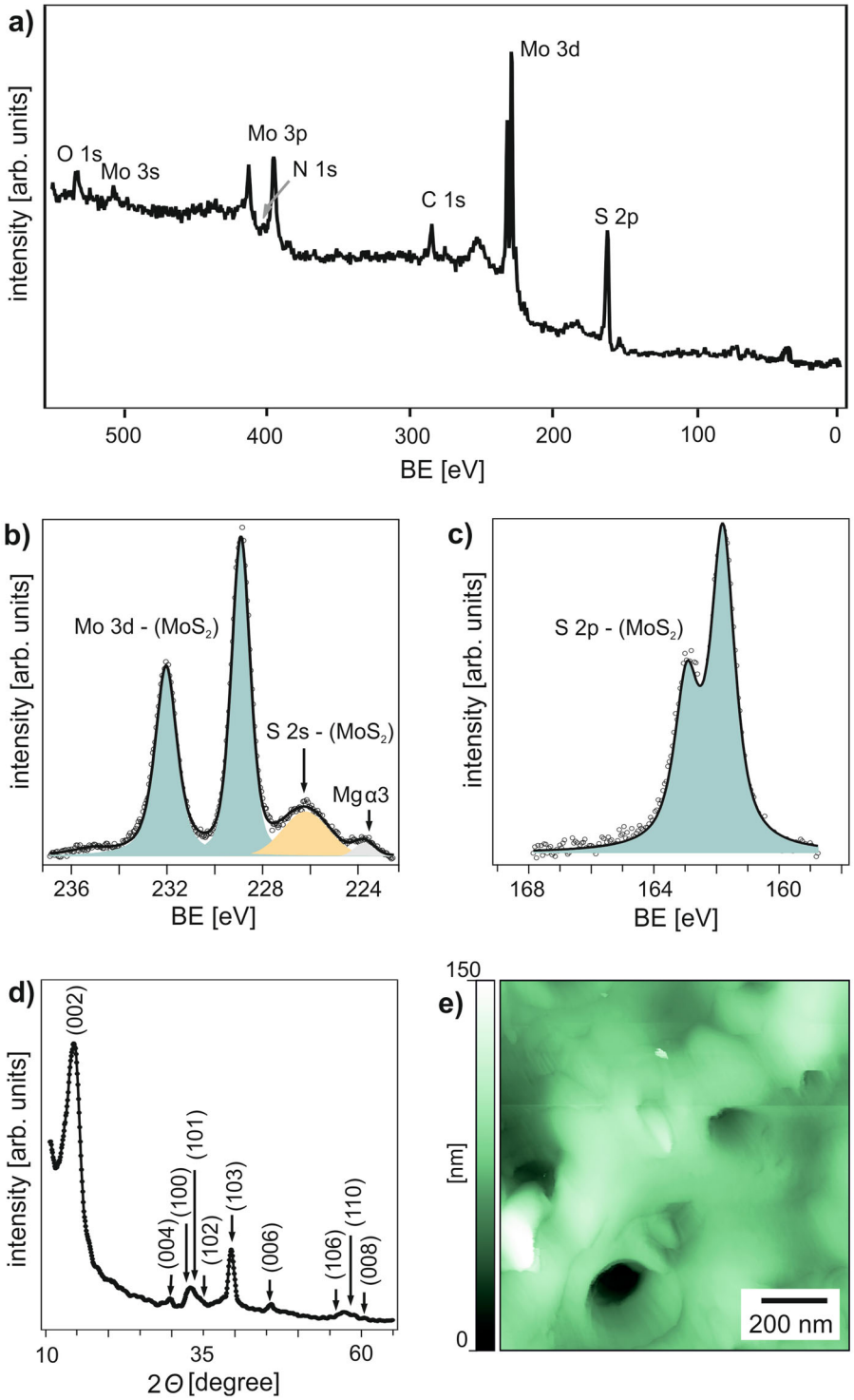

Fig. 1 Chemical and morphological properties. (a) XPS survey, fitted (**b**) Mo 3d−S 2s and (**c**) S 2p core-level spectra of large-area MoS_2 thin film grown via ionized jet deposition (IJD) and post-deposition annealed at 250 °C; corresponding (**d**) XRD spectrum and (**e**) AFM height image.

different values have been measured on the annealed samples (see Supplementary Fig. 3d), they are systematically smaller than 25.0 cm^{-1} with a minimum measured difference of 19.3 cm^{-1}. The Raman measurements confirm the PL data, indicating the remarkable capability of the MoS_2 thin films to display properties typical for 2D MoS_2.

Structural and electronic properties

To further prove how the annealed MoS_2 thin film displays typical 2D features, despite being thicker than 2D, a combination of transmission electron microscopy (TEM) and scanning tunnelling microscopy (STM) was employed to explore the structural and morphological properties. The bright-field TEM image in Fig. 3a

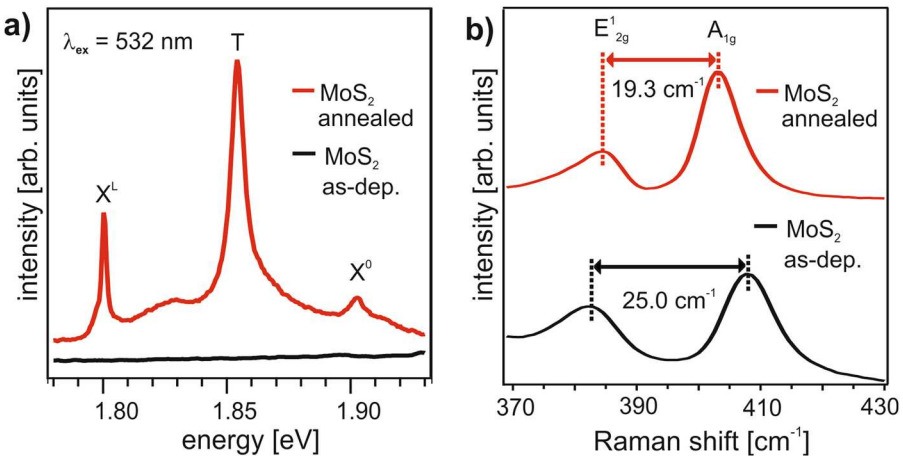

Fig. 2 Optical properties. (a) Photoluminescence (PL) and (**b**) non-resonant Raman ($\lambda = 532$ nm) spectra of as-deposited sample and annealed MoS_2 thin film.

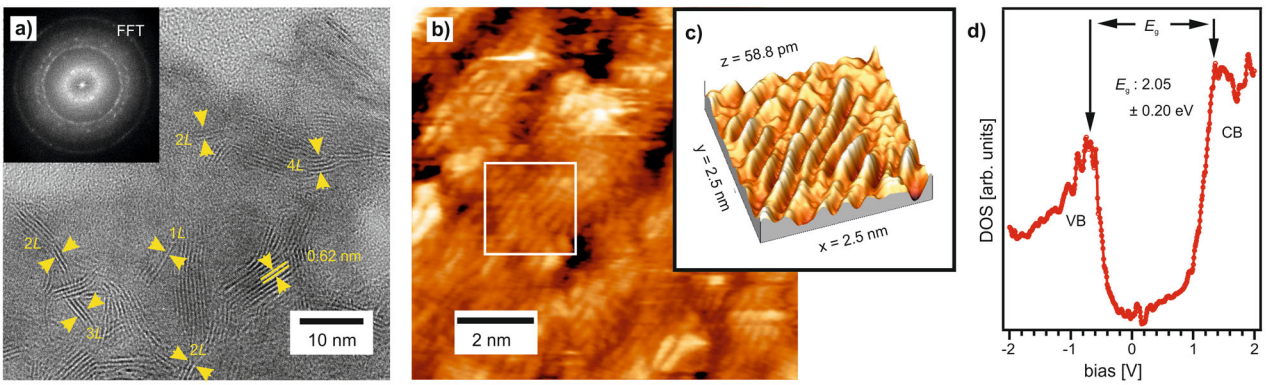

Fig. 3 Structure and electronic gap. (a) High-resolution TEM image (FFT image in the inset) and (**b**) STM image ($V_{bias} = -1.1$ V, 1.0 nA) of the MoS_2 thin film; (**c**) 3D height profile extracted from the region as marked in panel (**b**); (**d**) corresponding STS spectrum.

shows the presence of crystalline MoS_2 nanosheets surrounded by amorphous regions over the entire area. The ring pattern of the corresponding fast Fourier transform (FFT) image (inset of Fig. 3a) indicates that the individual crystalline nanosheets exhibit different orientations. From the two more intense inner rings interplanar distances of 0.62 and 0.27 nm are measured, corresponding to the (002) and (100) planes of hexagonal MoS_2 (JCPDS card 37-1492). The number of MoS_2 layers (L) in an individual nanosheet, whose stacking periodicity is 0.62 nm[50], is mainly in the range of 1–4 L.

In Fig. 3b, a typical STM image of the MoS_2 thin film is depicted. A riffled structure corresponding to protruding nanosheets can be seen, which becomes more obvious in the 3D height profile in Fig. 3c. FFT analysis of an atomic-resolution STM image (see Supplementary Fig. 4) gives a surface periodicity of 0.28 nm, in good agreement with the sulfur-to-sulfur distance between individual MoS_2 layers.

Figure 3d shows the local density of states (DOS) obtained by scanning tunnelling spectroscopy (STS) taken on the surface shown in Fig. 3c. The DOS is obtained by averaging over 30 different curves and then following the procedure described in ref. [51] to remove the exponential dependence on the tunnelling transmission probability of the electrons. This procedure avoids problems of obtaining a wide dynamic range in the tunnelling current which in general is a limiting factor in determining bandgap on semiconducting surfaces[51,52]. Thus, the obtained bandgap is (2.05 ± 0.20) eV, which lies within the range of previously reported STS bandgaps of 2D MoS_2[53–55]. The Fermi Level position lies in the lower half of the bandgap indicating a p-type character of the material.

The surface electronic properties of the MoS_2 thin film on Pt were further investigated by electron energy loss spectroscopy (EELS) and ultraviolet photoemission spectroscopy (UPS), see Fig. 4. The optical bandgap E_g of the MoS_2 thin film was measured by EELS (see red curve Fig. 4a). The corresponding EELS spectrum of the thin film before annealing (i.e., amorphous as-deposited sample) can be found in Supplementary Fig. 5a, however, it cannot be considered as a reference for the electronic properties of stoichiometric and crystalline MoS_2 (neither 3D nor 2D). Thus, we compare the annealed sample with a 3D MoS_2 single crystal serving as a crystalline bulk reference (see blue curve in Fig. 4a). Furthermore, it should be noted that the exciton BE for MoS_2 grown on metal substrates is typically less than 0.1 eV[56], therefore, optical and electronic bandgaps nearly coincide for the present MoS_2 thin film deposited on Pt. For the reference sample, E_g is found to be 1.30 eV, in good agreement with previously reported EELS of bulk MoS_2[57], whereas for the annealed MoS_2 thin film E_g is found to be 1.86 eV. This value is comparable to the one measured for 2D MoS_2 displaying a direct bandgap[58]. Hence, the results obtained from STS and EELS confirm the Raman and PL findings of the 2D character of the annealed thin films despite its thickness of ~200 nm, and support the presence of few-layered 2D MoS_2 nanosheets (as observed by TEM).

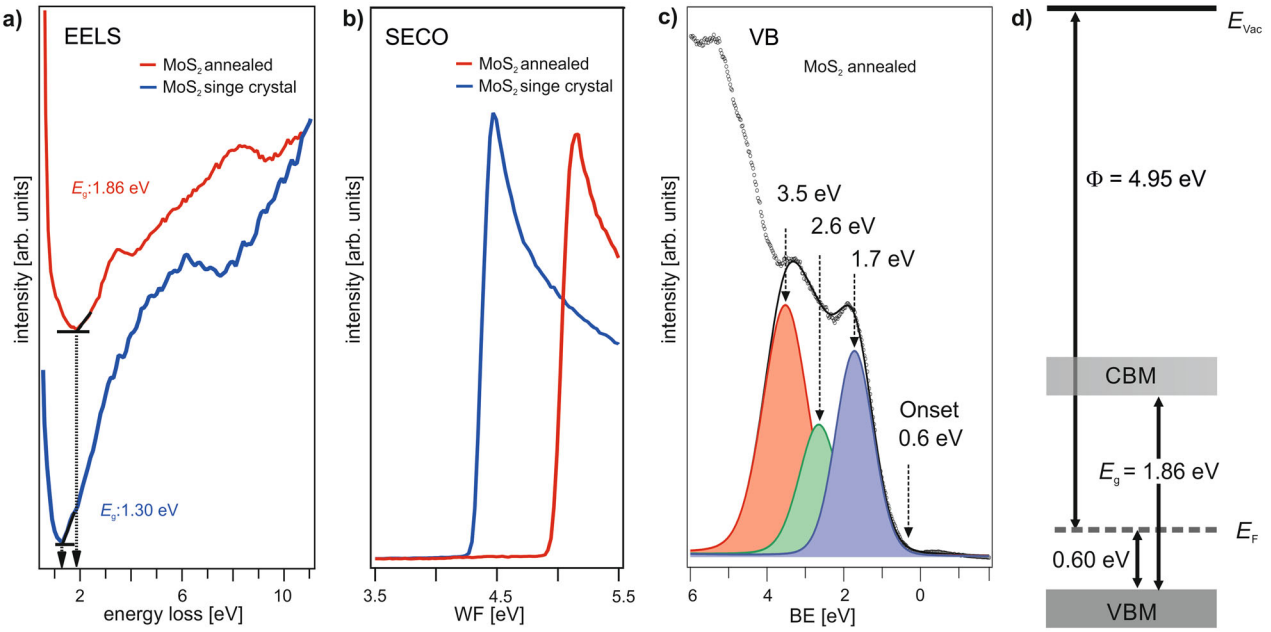

Fig. 4 Electronic properties. (a) EELS and (**b**) SECO spectrum of the MoS_2 thin film compared to the spectrum of a MoS_2 reference (single crystal); (**c**) corresponding valence band (VB) region UPS spectrum and (**d**) energy-level diagram. The energetic positions of the vacuum level (VL), the work function Φ, and VBM relative to the Fermi level E_F were determined by UPS measurements, whereas the energy gap E_g was derived by EELS.

The work function (Φ) obtained by the secondary electron cut off (SECO) shown in Fig. 4b, is Φ = 4.95 eV for the MoS_2 thin film and of Φ = 4.33 eV for the reference MoS_2 crystal, suggesting a more p-type nature[59] of the thin film compared to the reference. This is also demonstrated by the valence band maximum (VBM) observed at about 0.6 eV, hence locating the Fermi level E_F (BE = 0 eV) in the lower half of the bandgap, as also detected by the STS measurements (Fig. 3d), which is consistent with p-type behaviour[59]. The VB line shape is comparable to the one reported for MoS_2 single crystal[60] and other synthesized MoS_2[20,25,61], and displays two-component centred at 1.7 and 3.5 eV, resulting from Mo 4d−S 3p hybridized orbitals[62,63]. A third minor component centred at 2.6 eV (green peak in Fig. 4c) is related to the presence of surface dangling bonds[64–66]. Figure 4d displays the resulting energy band diagram of the MoS_2 thin film as derived by EELS and UPS measurements.

Device characterization

To evaluate the electrical performance of the MoS_2 thin film and to prove the versatile applicability of the herein reported IJD deposition technique for electronic components, we fabricated MoS_2-based resistive random memory (ReRAM) devices, which are typically defined by an abrupt change in the material's resistivity after applying external voltages. Cylindrical Au electrodes (400 µm in diameter) were deposited on a Si_3N_4-on-quartz substrate integrating contact lines for external connection to perform the electrical characterization, as displayed in Fig. 5a–c. The optical micrograph and SEM image in Fig. 5a, b, respectively, display the Au bottom electrodes present on the substrate for subsequent MoS_2 thin film and Au top-contact deposition. The cross-section of the final device architecture is schematically shown in Fig. 5c. Electrical characterization was carried out by contacting the line connected to the bottom electrode and the top electrode with two tungsten tips of a probe station. Current vs bias (I−V) curves were acquired by voltage sweep (0 V → 5 V → 0 V) while measuring the current through the devices. This leads to abrupt resistivity changes of the MoS_2 film, as displayed in Fig. 5d. At the beginning of the sweep (i), linear I−V behaviour is observed with constant resistance of 1.66 × 105 Ω. At a threshold voltage, the current increases abruptly (ii and iii) up to a pre-set compliance level (100 µA). During the back sweep (iii) the current stays at compliance level past the threshold level. A state of low resistivity is reached at 1.55 × 103 Ω. Reversibility is demonstrated by applying a reverse-biased voltage sweep without current compliance, as displayed in Fig. 5e. An abrupt decrease of current is observed, returning the device to its previous high resistive state. Switching between both resistive states is demonstrated with an ON−OFF ratio of $>10^2$. The observed I−V characteristics are similar to behaviour reported for ReRAM based on MoS_2 fabricated by other techniques[20,67–69].

DISCUSSION

The MoS_2 thin films presented here exhibit optical and electronic properties (i.e., bandgap E_g = 1.86 eV) similar to 2D MoS_2, even though they are few hundreds of nm thick, large-area and continuous MoS_2 films. The findings can be ascribed to the fact that the large-area thin films are composed of randomly oriented luminescent and p-doped 2D MoS_2 nanosheets embedded in amorphous MoS_2. The simple model shown in Fig. 6 accounts for the MoS_2 nanosheet formation. Upon IJD, molecular-sized species with undefined stoichiometry Mo_xS_y ablate from the MoS_2 target (see IJD details in Supplementary Fig. 1) and condense on the substrate forming an amorphous film of S-enriched Mo_xS_y nanoclusters (see Fig. 6a) over the entire deposited area. The typical atomic arrangement of as-deposited Mo_xS_y nanoclusters is depicted in the enlarged view in Fig. 6a. Mo and S atoms initially form various chemical species (e.g., Mo−S−S−Mo, Mo−Mo−S, Mo−S−S) with a high number of defects, dangling bonds, and different chemical environments of the Mo atoms, as evidenced by detailed XPS core-level analysis of the as-deposited thin film (see Supplementary Fig. 1). Residual gas atoms such as C, N, and O, as schematically represented by the red atoms in Fig. 6a, are present in trace amounts during deposition due to the relatively

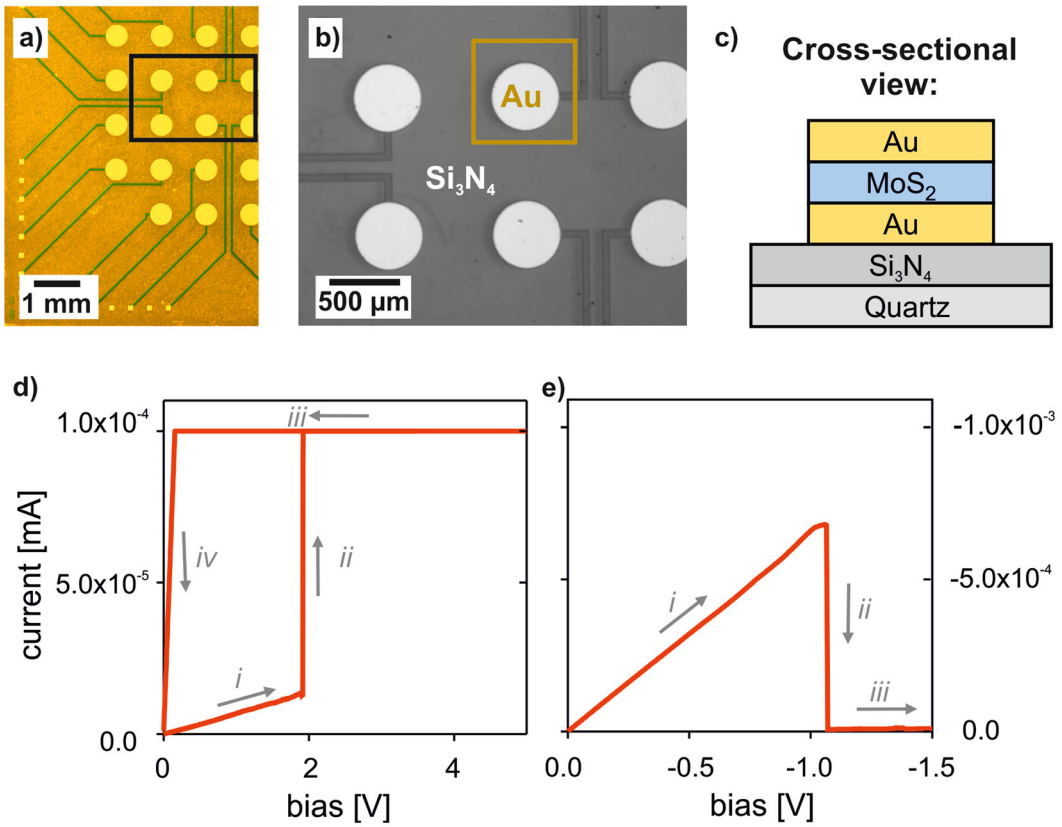

Fig. 5 Device characterization. (a) Optical micrograph of the pre-patterned Si_3N_4-on-quartz substrate used for MoS_2-based device fabrication; (**b**) SEM image of the region marked in (**a**); (**c**) schematic illustration of the device's cross-section (region marked in (**b**)) after deposition/annealing of the MoS_2 thin film and evaporation of the gold top-contact; *I*–*V* curve measurements of MoS_2-based device: (**d**) voltage sweep 0 V→5 V→0 V and (**e**) reversed bias sweep. The arrows indicate the voltage sweep progression during *I*–*V* measurements.

low base vacuum of the IJD apparatus (10^{-7} mbar). The post-deposition annealing at 250 °C favours the rearrangement of Mo_xS_y species into layered crystalline 2D MoS_2 nanosheets within the nanoclusters composing the thin film (Fig. 6b), as evidenced by TEM and STM analysis (see Fig. 3). Due to the nature of the growth process, we expect that the 2D MoS_2 nanosheets exhibit atomic defects such as Mo and S vacancies (represented by red-circled grey atoms in Fig. 6b) and that C, N, and O residual gas atoms are incorporated into the MoS_2 crystal structure (represented by red atoms in Fig. 6b). Since XPS analysis shows no extra peak in the Mo 3d and S 2p core levels (Fig. 1b, c) resulting in an overall atomic ratio S/Mo of ~2, we assume that also the amorphous encapsulation matrix (light green in Fig. 6b) exhibits a final stoichiometric composition of MoS_2. Even though the film is composed of two MoS_2 phases, namely crystalline nanosheets and amorphous matrix, the materials' electronic and optical properties are dominated by the 2D MoS_2 nanosheets (see Figs. 1, 2, and 4). The remaining amorphous phase does not contribute to the observed properties, but only serves as encapsulation/passivation material.

Note that the XPS core levels of the annealed MoS_2 thin film are shifted to lower BEs (by 0.6 eV) with respect to the as-deposited sample (Supplementary Fig. 1b, c). Such BE shifts can be related to two different processes; first, the formation of MoS_2 nanostructures was previously found to result in shifts to lower BEs with respect to the bulk values[70], which is in agreement with the present MoS_2 nanosheet formation. Second, the annealing leads to a strong change of the electronic properties of the MoS_2 thin film. The VBM at 0.6 eV below E_F (Fig. 4c), the increased work function (4.95 eV), and the bandgap of 1.86 eV indicate that the crystalline MoS_2 nanosheets exhibit p-type behaviour[71] (see the position of E_F in Fig. 4d). It has been reported that encapsulation of 2D MoS_2 can effectively lower the position of E_F[45], which is in agreement with our finding of p-type doping of encapsulated 2D MoS_2 nanosheets. Moreover, unsaturated sulfur vacancies effectively induce p-type behaviour when they are not backfilled, e.g., when the vacancy-rich MoS_2 surface is kept under UHV conditions[66]. Since encapsulation prevents the reaction with ambient gases[44–46], we assume that the p-type doping of encapsulated 2D MoS_2 nanosheets is mainly related to unsaturated vacancies.

A second mechanism that can induce p-type doping might be related to residual gas atoms that either react with some of the vacancies leading to the incorporation of substitutional/interstitial C, N, and O atoms into the MoS_2 lattice[59,72,73] (even though undetectable via XPS) or induce charge transfer[74,75] due to adsorption at the MoS_2 nanosheet surface.

The most striking feature of the crystalline 2D MoS_2 nanosheets is the observed bandgap of 1.86 eV (Figs. 3d and 4a) comparable to the one found for monolayer MoS_2, and a well-resolved PL signal (Fig. 2) with the most prominent peak stemming from charged excitons (T). The high intensity of the T peak with respect to the neutral X^0 is in good agreement with our finding of p-type behaviour (high-density charged carriers)[44]. Up to date, such narrow PL emissions were only measured at low temperatures (4–10 K), for encapsulated monolayer MoS_2[44–47]. In the present study, the detection of very narrow optical emission signals at room temperature might be related to the fact that the p-doped 2D MoS_2 nanosheets are highly crystalline but with local atomic defects (e.g., Mo and S vacancies), which act as a source of high-density charged carriers/photon emitters encapsulated in amorphous MoS_2. On one hand, the amorphous MoS_2 encapsulation

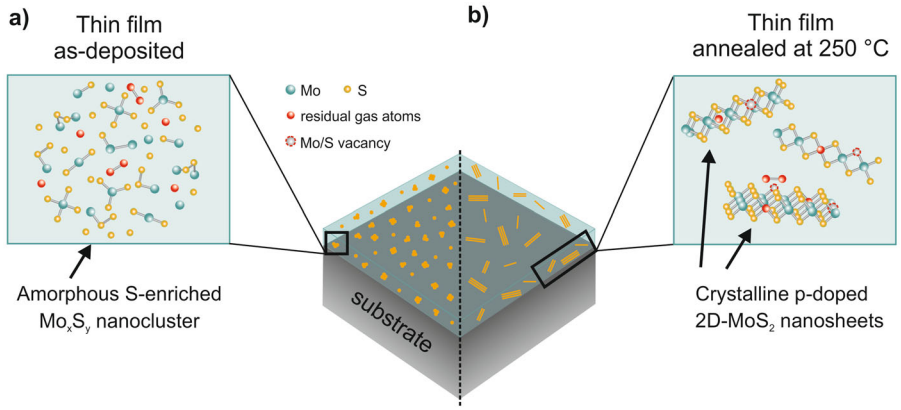

Fig. 6 Schematic illustration of thin film growth. (a) Mo_xS_y nanoclusters in the as-deposited thin film and (**b**) few-layered crystalline 2D-MoS_2 nanosheets in the annealed thin film (amorphous MoS_2 matrix is represented in light green); the enlarged view depicts the corresponding atomic arrangement of as-deposited sample and annealed MoS_2 thin film, respectively.

electrically shields the individual nanosheets from each other and prevents interaction with the substrate (i.e., no extrinsic doping or charge transfer from the substrate), therefore reducing electric field fluctuations[44] and consequently suppressing related inhomogeneous contributions to the exciton linewidth. On the other hand, as the crystalline 2D MoS_2 nanosheets maintain embedded during their growth, they are protected against physisorption of impurities from the environment[45,46], allowing to keep the locally disordered structure of the nanosheets (e.g., Mo and S vacancies) that is likely responsible for the sharp PL emission (T and X^L peaks in Fig. 2a).

It should be noted that the relatively low annealing temperature of 250 °C was chosen to grow thin films compatible with polymer-based electronics and to avoid complete crystallization of the material, as the presence of the amorphous MoS_2 matrix is expected to stabilize and passivate the luminescent few-layered 2D-MoS_2 nanosheets. Different to single-phase materials such as exfoliated and CVD-grown flakes, the IJD-derived composite material (i.e., the 2D-MoS_2 nanosheets encapsulated in amorphous MoS_2) is expected to have stable optical and electronic properties over time, hence ensuring the quality of the thin films even after months.

The realized ReRAM device with an abrupt ON/OFF ratio of more than two orders of magnitude finally proves the excellent qualities of the MoS_2 nanosheet-containing thin film as a semiconductor material for electronic applications. It is important to note that the MoS_2 thin film works as a whole and not via single 2D-MoS_2 nanosheets. In other words, the dimensions of the metal contacts for device fabrication are large enough to ensure that the electrical behaviour is averaged over an area larger than a single MoS_2 nanosheet, proving that the amorphous MoS_2 encapsulation is conductive enough for device operation. The device was stable over dozens of cycles and reproducible in terms of retention time over a few days, highlighting the possibility to perform multicycle writing and reset operations. The growth of a stable 3D bulk material with 2D MoS_2 properties makes the IJD technique an excellent candidate for practical use in optoelectronic devices.

In the present study, we showed that IJD is able to efficiently grow MoS_2 thin films over inches-wide areas required for industrial up-scalable deposition. Crystalline 2D MoS_2 nanosheets encapsulated in an amorphous MoS_2 shell compose the film after a post-annealing step at low temperatures (i.e., 250 °C). This makes the IJD technique compatible with all substrates and/or supports typically used for (opto-)electronic applications, including the family of flexible polymeric materials used for displays, wearable electronics, etc.

The as-deposited Mo_xS_y nanoclusters rearrange after annealing and form highly crystalline 2H-MoS_2 nanosheets encapsulated in amorphous MoS_2. The material exhibits a bandgap of 1.86 eV and excellent photoluminescence properties, comparable to those reported for encapsulated single-layer MoS_2. The MoS_2 thin films were shown to be applicable in ReRAM devices with low erasing and writing voltage thresholds.

In contrast to MoS_2 grown via other techniques, where an increase in thickness of more than a few layers unavoidably leads to the loss of the desired optical and electronic properties, the MoS_2 thin films grown by IJD containing few-layered crystalline 2D-MoS_2 nanosheets show properties comparable to few-layer 2H-MoS_2 even over a large area and independent on the film thickness. This is due to the encapsulation of the crystalline MoS_2 nanosheets (responsible for the 2D properties) in an amorphous MoS_2 matrix, forming a mechanically stable two-phase thin film (bulk). The 2D-embedded-in-bulk composition of the thin film ensures easier handling and makes the IJD technique preferential for mass production of electronic devices, where the fabrication process must be simplified as much as possible to guarantee low costs, but at the same time keep high-quality material and production standards.

In addition, the IJD technique enables the possibility to work with selenide-based TMDCs, such as WSe_2, $NbSe_2$, etc., ensuring the right composition of the thin films without the need of highly toxic selenium in the gas phase. Different from other deposition techniques, where multi-step processes are required to fabricate TMDC heterostructures, the IJD technique paves the way to one-solution *in-situ* multi-target deposition for TMDC heterostructures with desired electronic, optical, and magnetic properties.

METHODS

Ionized jet deposition of MoS_2 thin films

Unless otherwise stated, the present MoS_2 thin films were grown on Pt (50 nm)-on-Si substrates (see ref. [76] for details of substrate preparation) to avoid self-oxidation and sulfur interaction with the substrate. The IJD growth was carried out at room temperature in a lab-grade IJD system through the ablation of a cylindrical MoS_2 target (Testbourne Ltd., Ø = 5 cm, thickness = 0.5 cm) with a target-to-substrate distance of 150 mm, a base pressure of $p \sim 10^{-7}$ mbar, and using Ar as working gas (during deposition: $p = 10^{-3}$–10^{-5} mbar). The IJD discharge parameters were set at $f = 150$ Hz and $V = 15$ kV, with a total deposition time of 1 h. The as-deposited thin films were subjected to HV ($p = 1 \times 10^{-6}$ mbar) post-deposition annealing at $T = 250$ °C for 3 h. Electrical characterization was carried out on electronic devices that were fabricated by deposition of annealed MoS_2 thin films on Si_3N_4-on-quartz substrates. The substrates were pre-patterned with Au pads (Ø = 500 µm) serving as

bottom-contacts. Before MoS_2 deposition, the pre-patterned Si_3N_4 substrates were masked with polymethyl methacrylate (PMMA), leaving the Au bottom-contacts uncovered for subsequent MoS_2 and Au top-contact deposition. In a final step, the PMMA was peeled off.

Characterization

The thickness of the annealed MoS_2 thin films was determined via cross-sectional SEM images (e.g., see inlet in Supplementary Fig. 2d). Photoluminescence (PL) and non-resonant Raman spectra of as-deposited and annealed MoS_2 thin films were acquired using a LabRAM Aramis (Horiba Jobin-Yvon) instrument, which is equipped with an optical microscope and a 100× objective. A diode-pumped solid-state laser source of 532 and 632 nm was used for the excitation of the PL and Raman signals. The luminescence and Raman signals were monitored with an air-cooled charge-coupled device. The slit width of the spectrometer was typically set at 100 µm. A diffraction grating with 1800 lines mm^{-1} was used for the collection of all Raman spectra with an overall spectral resolution of ~2 cm^{-1}. PL and Raman spectra were collected with an overall acquisition time of 10 s by setting the laser power to 200 µW.

Ultraviolet photoelectron spectroscopy (UPS) was carried out using the He I photon with an energy at ~21.2 eV, and X-ray photoelectron spectroscopy (XPS) was performed with a non-monochromatized Mg Kα source (emission line at 1253.6 eV). The photoelectron signals were detected with a VSW HSA100 hemispherical analyzer equipped with PSP electronic power supply and control. The total energy resolution is about 0.1 eV for UPS and 0.8 eV for XPS. The binding energy (BE) scale of UPS spectra was referred to the Fermi level of the same Au clean substrate, whereas XPS BEs were calibrated using the Au 4f peak at 84.0 eV as reference. The SECO spectra were measured with a sample bias of −7.0 V.

EELS was performed with a Leybold electron gun (EQ22/35) operated at 1000 eV of primary beam energy and a CLAM2 (VG Microtech) electron analyzer, with a resolution of 0.1 eV. The electron beam current on the sample was 2 nA.

XRD spectra were detected with a Rigaku D/max III diffractometer in glancing incidence configuration, using Cu Kα radiation and a graphite monochromator in the diffracted beam. An asymmetric scan geometry was adopted to enhance the signal stemming from the MoS_2 thin film. Typical measurements were performed in the (2θ) range of 10−70° with an incidence angle of 1°, sampling interval of 0.05°, and counting time of 8 s.

For TEM analysis, the annealed MoS_2 thin film was transferred from the substrate by gently rubbing on standard carbon-coated copper grids. Samples were imaged with a field-emission JEM-2200FS JEOL TEM equipped with an in-column Omega filter operated at 200 kV.

The STM images were acquired in an UHV ($p < 10^{-10}$ mbar) chamber in constant current mode at room temperature, using an Omicron multiscan system. The Pt/Ir tip was prepared by electrochemical etching in saturated $CaCl_2$ aqueous solution and subsequently cleaned in UHV by electron bombardment. Before the measurements, all samples were degassed at approximately 120 °C at a pressure below 5×10^{-10} mbar for a minimum of 3 h up to 10 h and subsequently moved to the scanner without breaking the vacuum. The STM images were recorded in constant current mode with the tip to sample bias ranging from −0.7 to −2 V and tunnelling current ranging from 0.5 to 2 nA.

STS data were taken by the sample-and-hold technique at room temperature. For each point, the *I*/*V* and the d*I*/d*V* curves were collected. The d*I*/d*V* curve was obtained by applying to the bias potential, a modulating voltage of 20 mV, and collecting the derivative with a lock-in amplifier. The stabilizing conditions for the different points are V_{bias} in the −1.6−2.0 V range, *I* in the −0.5−2.0 nA range. Each curve was obtained by averaging over more than 20 individual spectra to improve the signal-to-noise ratio. The DOS was calculated following eq. 3 of ref. [51], e.g., from the (d*I*/d*V*)/(*I*/*V*), that is independent of the tip to sample distance.

Electrical characterization (current−voltage (*I*−*V*) measurements) of annealed MoS_2 thin films deposited on Au-covered Si_3N_4-on-quartz substrates were acquired at room temperature and in the air using an Imina miBots probe station with Tungsten tips connected to a Keithley 4200 A parameter analyzer.

DATA AVAILABILITY

The data that support the findings of this study are available from the corresponding author upon reasonable request.

Received: 2 March 2021; Accepted: 13 May 2021;
Published online: 07 July 2021

REFERENCES

1. Radisavljevic, B., Radenovic, A., Brivio, J., Giacometti, V. & Kis, A. Single-layer MoS2 transistors. *Nat. Nanotechnol.* **6**, 147–150 (2011).
2. Mak, K. F., Lee, C., Hone, J., Shan, J. & Heinz, T. F. Atomically thin MoS2: a new direct-gap semiconductor. *Phys. Rev. Lett.* **105**, 136805 (2010).
3. Ganatra, R. & Zhang, Q. Few-layer MoS2: a promising layered semiconductor. *ACS Nano* **8**, 4074–4099 (2014).
4. Samadi, M. et al. Group 6 transition metal dichalcogenide nanomaterials: synthesis, applications and future perspectives. *Nanoscale Horiz.* **3**, 90–204 (2018).
5. Gao, M. R., Xu, Y. F., Jiang, J. & Yu, S. H. Nanostructured metal chalcogenides: synthesis, modification, and applications in energy conversion and storage devices. *Chem. Soc. Rev.* **42**, 2986–3017 (2013).
6. Benck, J. D., Hellstern, T. R., Kibsgaard, J., Chakthranont, P. & Jaramillo, T. F. Catalyzing the hydrogen evolution reaction (HER) with molybdenum sulfide nanomaterials. *ACS Catal.* **4**, 3957–3971 (2014).
7. Theerthagiri, J. et al. Recent advances in MoS2 nanostructured materials for energy and environmental applications—a review. *J. Solid State Chem.* **252**, 43–71 (2017).
8. Liu, T. & Liu, Z. 2D MoS2 nanostructures for biomedical applications. *Adv. Healthc. Mater.* **1701158**, 1–18 (2017).
9. Zhu, X. et al. Intracellular mechanistic understanding of 2D MoS2 nanosheets for anti-exocytosis—enhanced synergistic cancer therapy. *ACS Nano* **12**, 2922–2938 (2018).
10. Yadav, U. et al. Enhanced osteogenesis by molybdenum disulfide nanosheet reinforced hydroxyapatite nanocomposite scaffolds. *ACS Biomater. Sci. Eng.* **5**, 4511–4521 (2019).
11. Magda, G. Z. et al. Exfoliation of large-area transition metal chalcogenide single layers. *Sci. Rep.* **5**, 14714 (2015).
12. Backes, C. et al. Guidelines for exfoliation, characterization and processing of layered materials produced by liquid exfoliation. *Chem. Mater.* **29**, 243–255 (2017).
13. Zhang, J. et al. Reversible and selective ion intercalation through the top surface of few-layer MoS2. *Nat. Commun.* **9**, 1–9 (2018).
14. Lee, Y.-H. et al. Synthesis of large-area MoS2 atomic layers with chemical vapor deposition. *Adv. Mater.* **24**, 2320–2325 (2012).
15. Dumcenco, D. et al. Large-area epitaxial monolayer MoS2. *ACS Nano* **9**, 4611–4620 (2015).
16. Chiu, M. et al. Determination of band alignment in the single-layer MoS2/WSe2 heterojunction. *Nat. Commun.* **6**, 7666 (2015).
17. George, A. S. et al. Wafer scale synthesis and high resolution structural characterization of atomically thin MoS2 layers. *Adv. Funct. Mater.* **24**, 7461–7466 (2014).
18. Lim, Y. R. et al. Wafer-scale, homogeneous MoS2 layers on plastic substrates for flexible visible-light photodetectors. *Adv. Mater.* **28**, 5025–5030 (2016).
19. Zheng, W. et al. Patterned growth of P-type MoS2 atomic layers using sol-gel as precursor. *Adv. Funct. Mater.* **26**, 6371–6379 (2016).
20. Nardi, M. V. et al. Versatile and scalable strategy To grow sol−gel derived 2H-MoS2 thin films with superior electronic properties: a memristive case. *ACS Appl. Mater. Interfaces* **10**, 34392–34400 (2018).
21. Mutz, N. et al. Pulsed thermal deposition of binary and ternary transition metal dichalcogenide monolayers and heterostructures. *Appl. Phys. Lett.* **114**, 162101 (2019).
22. Siegel, G., Venkata Subbaiah, Y. P., Prestgard, M. C. & Tiwari, A. Growth of centimeter-scale atomically thin MoS2 films by pulsed laser deposition. *APL Mater.* **3**, 056103 (2015).
23. Serna, M. I. et al. Large-area deposition of MoS2 by pulsed laser deposition with in situ thickness control. *ACS Nano* **10**, 6054–6061 (2016).
24. Tumino, F., Casari, C. S., Passoni, M., Russo, V. & Li Bassi, A. Pulsed laser deposition of single-layer MoS2 on Au(111): from nanosized crystals to large-area films. *Nanoscale Adv.* **1**, 643–655 (2019).
25. Tao, J. et al. Growth of wafer-scale MoS2 monolayer by magnetron sputtering. *Nanoscale* **7**, 2497–2503 (2015).
26. Hussain, S. et al. Large-area, continuous and high electrical performances of bilayer to few layers MoS2 fabricated by RF sputtering via post-deposition annealing method. *Sci. Rep.* **6**, 1–13 (2016).
27. Lotti, R., Nozar, P. & Taliani, C. Device for generating plasma and for directing a flow of electrons towards a target. WO 2010/109297 A3 (2010).
28. Skocdopolova, L. Device for generating plasma and directing an electron beam towards a target. WO 2013/186697 A2 (2013).

29. Skocdopolova, L. Un Apparato ed un Metodo per la Generazione di Elettroni e di Plasma da un Getto di Gas. ITBO 20120320 A1 (2013).
30. Ghiami, A., Timpel, M., Chiappini, A., Nardi, M. V. & Verucchi, R. Synthesis of MoS2 thin film by ionized jet deposition: role of substrate and working parameters. *Surfaces* **3**, 683–693 (2020).
31. Little, P. F. & von Engel, A. The hollow-cathode effect and the theory of glow discharges. *Proc. R. Soc. A* **224**, 209–227 (1954).
32. Skocdopole, J. et al. Preparing of the chameleon coating by the ion jet deposition method.*Acta Polytech. CTU Proc.* **9**, 19–25 (2017).
33. Gambardella, A., Berni, M., Russo, A. & Bianchi, M. A comparative study of the growth dynamics of zirconia thin films deposited by ionized jet deposition onto different substrates. *Surf. Coat. Technol.* **337**, 306–312 (2018).
34. Menossi, D. et al. SNS by ionized jet deposition for photovoltaic applications. *IEEE 44th Photovolt. Spec. Conf. (PVSC)*, Washington, DC, USA, 2372–2375 (2017).
35. Skočdopole, J., Kalvoda, L., Nozar, P. & Netopilík, M. Preparation of polymeric coatings by ionized jet deposition method. *Chem. Pap.* **72**, 735–1739 (2018).
36. Bianchi, M. et al. Plasma-assisted deposition of bone apatite-like thin films from natural apatite. *Mater. Lett.* **199**, 32–36 (2017).
37. Liguori, A., Gualandi, C., Focarete, M. L., Biscarini, F. & Bianchi, M. The pulsed electron deposition technique for biomedical applications: a review. *Coatings* **10**, 1–19 (2020).
38. Gao, D. et al. Ferromagnetism in freestanding MoS2 nanosheets. *Nanoscale Res. Lett.* **8**, 129 (2013).
39. Fan, X. et al. Fast and efficient preparation of exfoliated 2H MoS2 nanosheets by sonication-assisted lithium intercalation and infrared laser-induced 1T to 2H phase reversion. *Nano Lett.* **15**, 5956–5960 (2015).
40. Splendiani, A. et al. Emerging photoluminescence in monolayer MoS2. *Nano Lett.* **10**, 1271–1275 (2010).
41. Zheng, B. & Chen, Y. Controllable growth of monolayer MoS2 and MoSe2 crystals using three-temperature-zone furnace. *IOP Conf. Ser. Mater. Sci. Eng.* **274**, 012085 (2017).
42. Coehoorn, R., Haas, C. & De Groot, R. A. Electronic structure of MoSe2, MoS2, and WSe2. II. The nature of the optical band gaps. *Phys. Rev. B* **35**, 6203–6206 (1987).
43. Eda, G. et al. Photoluminescence from chemically exfoliated MoS2. *Nano Lett.* **11**, 5111–5116 (2011).
44. Ajayi, O. A. et al. Approaching the intrinsic photoluminescence linewidth in transition metal dichalcogenide monolayers. *2D Mater.* **4**, 031011 (2017).
45. Wierzbowski, J. et al. Direct exciton emission from atomically thin transition metal dichalcogenide heterostructures near the lifetime limit. *Sci. Rep.* **7**, 12383 (2017).
46. Cadiz, F. et al. Excitonic linewidth approaching the homogeneous limit in MoS2-based van der Waals heterostructures. *Phys. Rev. X* **7**, 021026 (2017).
47. Klein, J. et al. Atomistic defect states as quantum emitters in monolayer MoS2. *Nat. Commun.* **10**, 2755 (2019).
48. Li, H. et al. From bulk to monolayer MoS2: evolution of Raman scattering. *Adv. Funct. Mater.* **22**, 1385–1390 (2012).
49. Ottaviano, L. et al. Mechanical exfoliation and layer number identification of MoS2 revisited. *2D Mater.* **4**, 045013 (2017).
50. Deokar, G. et al. Toward the use of CVD-grown MoS2 nanosheets as field-emission source. *Beilstein J. Nanotechnol.* **9**, 1686–1694 (2018).
51. Feenstra, R. M., Stroscio, J. A. & Fein, A. P. Tunneling spectroscopy of the Si(111) 2 × 1 surface. *Surf. Sci.* **181**, 295–306 (1987).
52. Feenstra, R. M. & Stroscio, J. A. Tunneling spectroscopy of the GaAs (110) surface. *J. Vac. Sci. Technol. B* **5**, 923–929 (1987).
53. Rigosi, A. F., Hill, H. M., Rim, K. T., Flynn, G. W. & Heinz, T. F. Electronic band gaps and exciton binding energies in monolayer Mox W1-x S2 transition metal dichalcogenide alloys probed by scanning tunneling and optical spectroscopy. *Phys. Rev. B* **94**, 1–6 (2016).
54. Liu, X. et al. Rotationally commensurate growth of MoS2 on epitaxial graphene. *ACS Nano* **10**, 1067–1075 (2016).
55. Trainer, D. J. et al. Inter-layer coupling induced valence band edge shift in mono- to few-layer MoS2. *Sci. Rep.* **7**, 40559 (2017).
56. Park, S. et al. Direct determination of monolayer MoS2 and WSe2 exciton binding energies on insulating and metallic substrates. *2D Mater.* **5**, 025003 (2018).
57. Hong, J. et al. Layer-dependent anisotropic electronic structure of freestanding quasi-two-dimensional MoS2. *Phys. Rev. B* **93**, 075440 (2016).
58. Dileep, K., Sahu, R., Sarkar, S., Peter, S. C. & Datta, R. Layer specific optical band gap measurement at nanoscale in MoS2 and ReS2 van der Waals compounds by high resolution electron energy loss spectroscopy. *J. Appl. Phys.* **119**, 114309 (2016).
59. Azcatl, A. et al. Covalent nitrogen doping and compressive strain in MoS2 by remote N2 plasma exposure. *Nano Lett.* **16**, 5437–5443 (2016).
60. Coy Diaz, H., Addou, R. & Batzill, M. Interface properties of CVD grown graphene transferred onto MoS2(0001). *Nanoscale* **6**, 1071–1078 (2014).
61. Zhang, Z., Qian, Q., Li, B. & Chen, K. J. Interface engineering of monolayer MoS2/GaN hybrid heterostructure: modified band alignment for photocatalytic water splitting application by nitridation treatment. *ACS Appl. Mater. Interfaces* **10**, 17419–17426 (2018).
62. Lu, S.-C. & Leburton, J.-P. Electronic structures of defects and magnetic impurities in MoS2 monolayers. *Nanoscale Res. Lett.* **9**, 676 (2014).
63. Ahmad, S. & Mukherjee, S. A comparative study of electronic properties of bulk MoS2 and its monolayer using DFT technique: application of mechanical strain on MoS2 monolayer. *Graphene* **03**, 52–59 (2014).
64. Kunstmann, J., Wendumu, T. B. & Seifert, G. Localized defect states in MoS2 monolayers: electronic and optical properties. *Phys. Status Solidi* **8**, 1–20 (2016).
65. Pandey, M. et al. Defect-tolerant monolayer transition metal dichalcogenides. *Nano Lett.* **16**, 2234–2239 (2016).
66. Ghiami, A. et al. Unravelling work function contributions and their engineering in 2H-MoS2 single crystal discovered by molecular probe interaction. *J. Phys. Chem. C.* **124**, 6732–6740 (2020).
67. Yin, Z. et al. Memory devices using a mixture of MoS2 and graphene oxide as the active layer. *Small* **9**, 727–731 (2013).
68. Wang, W., Panin, G. N., Fu, X., Zhang, L. & Ilanchezhiyan, P. MoS2 memristor with photoresistive switching. *Sci. Rep.* **6**, 31224 (2016).
69. Cheng, P., Sun, K. & Hu, Y. H. Memristive behavior and ideal memristor of 1T phase MoS2 nanosheets. *Nano Lett.* **16**, 572–576 (2016).
70. Li, B. et al. Preparation of monolayer MoS2 quantum dots using temporally shaped femtosecond laser ablation of bulk MoS2 targets in water. *Sci. Rep.* **7**, 11182 (2017).
71. Lee, J. S., Park, C. S., Kim, T. Y., Kim, Y. S. & Kim, E. K. Characteristics of p-type conduction in P-doped MoS2 by phosphorous pentoxide during chemical vapor deposition. *Nanomaterials* **9**, 1278 (2019).
72. Chen, M. et al. Stable few-layer MoS2 rectifying diodes formed by plasma-assisted doping. *Appl. Phys. Lett.* **103**, 142110 (2013).
73. Luo, P. et al. Doping engineering and functionalization of two-dimensional metal chalcogenides. *Nanoscale Horiz.* **4**, 26–51 (2019).
74. Lee, S. Y. et al. Large work function modulation of monolayer MoS2 by ambient gases. *ACS Nano* **10**, 6100–6107 (2016).
75. Hu, C. et al. Work function variation of monolayer MoS2 by nitrogen-doping. *Appl. Phys. Lett.* **113**, 041602 (2018).
76. Prusakova, V. et al. Morphologic, structural, and optical characterization of sol-gel derived TiO2 thin films for memristive devices. *Phys. Status Solidi* **12**, 192–196 (2015).

ACKNOWLEDGEMENTS

We thank R. Ceccato for granting access to the XRD instrument and L. Lorenzelli for providing the Pt/Si and pre-patterned Si_3N_4-on-quartz substrates. L. G. and E. C. thank G. Drera for the support on STS curve elaboration. M. V. N. and M. T. gratefully acknowledge the support by the CARITRO Foundation (project MILA, grant no. 2017.0369), Trento (Italy). E. L. K. and G. L. acknowledge the support from the Helmholtz Energy Materials Foundry (HEMF) and PEROSEED (ZT-0024) project. G. L., F. G., and E. L. K. thank D. F. G. (Project No. 182087777-SFB 951) for the financial support. This work was carried out in the framework of the Joint Lab GEN_FAB.

AUTHOR CONTRIBUTIONS

Conceptualization, M. V. N., and R. V.; methodology, M. T. and M. V. N.; validation, M. V. N. and A. C.; investigation, A. G., G. L., F. G., L. G., E. C., P. N., F. R., and A. C.; resources, R. V., E. J. W. L, and A. Q.; writing—original draft preparation, M.T.; writing—review and editing, M. T., L. G., and R. V.; visualization, M. T. and M. V. N.; supervision, M. V. N. and R. V.; all authors have read and agreed to the published version of the paper.

COMPETING INTERESTS

The authors declare no competing interests.

ADDITIONAL INFORMATION

Supplementary information The online version contains supplementary material available at https://doi.org/10.1038/s41699-021-00244-x.

Correspondence and requests for materials should be addressed to M.T. or M.V.N.

Reprints and permission information is available at http://www.nature.com/reprints

Publisher's note Springer Nature remains neutral with regard to jurisdictional claims in published maps and institutional affiliations.